Including real fuel chemistry in Large-Eddy Simulations

Anne Felden[⋆][†] *Lucas Esclapez*[⋆] *Antony Misdariis*[⋆] *Eleonore Riber*[⋆] *Hai Wang*[‡]
and Bénédicte Cuenot[⋆]
⋆ *CERFACS, CFD Team*
42 Av. Gaspard Coriolis, 31057 Toulouse, France
‡ *Department of Mechanical Engineering*
Stanford University, Stanford, CA 94305, USA
felden@cerfacs.fr · esclapez@cerfacs.fr · misdariis@cerfacs.fr · riber@cerfacs.fr
haiwang@stanford.edu · cuenot@cerfacs.fr
[†]Corresponding author

Abstract

Large-eddy simulation (LES) is progressively becoming a crucial design tool for the next generation of aeronautical combustion chambers. However, further improvements of the capability of LES is required for predicting pollutant emissions. Indeed, the detailed description of fuel pyrolysis and oxidation requires to take into account hundreds of chemical species involved in the complex non-linear reaction process. The direct integration of such detailed chemistry in LES is not a viable path, because of excessive computational demands and numerical stiffness. Modeling real transportation fuel is further complicated by the fact that kerosenes are complex blends of a large number of hydrocarbon compounds; the exact composition of which is very difficult to determine. In this work, the real-fuel combustion chemistry is described by the Hybrid Chemistry (HyChem) approach; and an LES-compliant Analytically Reduced Chemistry (ARC) is used to allow a direct integration of the fuel chemistry in the LES solver. The ARC mechanism is coupled with the Dynamically Thickened Flame LES model (DTFLES) and a Lagrangian spray description to investigate the turbulent two-phase flow flame of a lean direct injection combustor, fueled with Jet-A. The LES results are compared to experimental data in terms of gas velocity, temperature and major species (CO_2, H_2O, CO, NO) mass fractions. It is found that the proposed methodology accurately predicts both the flow dynamics and pollutant formation, and presents therefore a great potential to study complex flame configurations burning real jet fuels.

1. Introduction

Large Eddy Simulation (LES) is now a widely used tool for the simulation of turbulent combustion in both academic and applied research. At the heart of combustion processes, fuel pyrolysis and oxidation usually proceed through complex and highly non-linear reaction mechanisms involving hundreds of chemical species. However, the direct integration of such detailed chemistry in LES is not a viable path, because of excessive computational demands and numerical stiffness. Employing a refined chemistry description may not be desirable either, as it involves a large number of reactions which individually contribute very little to the global flame behavior, while introducing possibly large uncertainties due to unknown parameters. In addition, detailed chemistry greatly complicates the modeling and analysis of the strong coupling between turbulence and chemistry.

In practice, combustion simulations use either globally fitted chemical mechanisms,[41] or pre-tabulated laminar flame solutions based on detailed chemistry.[16, 32, 33] Both methods are able to accurately predict global quantities such as laminar flame speed and burnt gas state, but have important, though different, limitations. Global mechanisms severely reduce the number of reaction parameters, and are therefore only valid over a narrow range of operating conditions. By construction, they are unable to directly describe pollutant chemistry or complex, multi-component fuels. On the other hand, pre-tabulated chemistry oversimplifies the interaction between the flame and the flow and taking into account complex phenomena such as dilution, slow pollutant chemistry or heat losses is far from straightforward and always case-dependant.

In an attempt to find the best compromise between complexity and accuracy in the context of LES, analytically reduced chemistries (ARC) have been introduced.[18] These mechanisms accurately describe combustion phenomena by retaining the most important species and reactions, in a physically-oriented way. ARC contain about 10 to 30 species

from methane to dodecane, are nowadays affordable on high-performance computers, and are non-stiff by construction. ARC use in LES of 3D configurations is still recent and has focused mostly on simple, single-component fuels such as methane or ethylene in academic configurations.[12, 14, 27] Unfortunately, the extension to realistic applications is complicated by the multicomponent nature of real-fuels and uncertainties concerning their oxidation pathways, as well as by the interactions with the multi-phase flow modeling.

Recently, an alternative approach to developing combustion chemistry models for real, multicomponent jet fuels was proposed.[43] The approach, termed HyChem, assumes that fuel pyrolysis is fast and decoupled from the oxidation of decomposed products. It relies on shock-tube and flow reactor experiments on a real fuel to derive the lumped reaction kinetic parameters for fuel pyrolysis and then uses a detailed reaction model to describe the oxidation of the handful of decomposed products. The resulting models have been shown to predict a wide range of global combustion properties, including the laminar flame speed, counterflow non-premixed flame extinction, and shock-tube ignition delay time. More importantly, it has been shown that deriving ARC of HyChem models comprised of about 30 species, that are still able to reproduce well the combustion chemistry behaviors of real fuels, is feasible.[13]

This paper presents the validation of a new methodology for performing LES of realistic combustors operated with real-fuels such as kerosene. This methodology combines the HyChem model with the ARC approach in a thickened flame framework in order to allow an explicit integration of the chemistry in the LES. First, the derivation and validation of an ARC for a specific Jet-A fuel are presented. Then the 3D configuration chosen to perform the LES is introduced, followed by a presentation of the governing equations and modeling framework. Finally the results obtained for the 3D turbulent simulation are presented and the accuracy of the methodology is assessed against experimental data in terms of gas velocity, spray characteristics and species distribution.

2. Derivation of an ARC for Jet-A with NO$_x$ chemistry

2.1 The Jet-A POSF10325 specifications

The fuel considered here is an average, commercial Jet-A fuel (POSF10325), which was procured from the Shell Mobile refinery in June 2013 as a part of tests conducted by the National Jet Fuel Combustion Program. Its properties are summarized in Table 1. For this fuel, a recent study by Edwards *et al.*[7] reports the derivation of two multi-component surrogates, constructed to match the H/C ratio, smoke point, and DCN. Employing one of these surrogates would require to consider three hydrocarbons representative of the main classes, along with their associated pathways, complexifying the reduction process.

Molecular formula	Composition (mass fraction [%])					Mol. Weight [kg/mol]
	Aromatics	*iso*-Paraffins	*n*-Paraffins	Cycloparaffins	Alkenes	
$C_{11.4}H_{22.1}$	18.66	29.45	20.03	31.86	<0.001	156.0
H/C	Δh_c [MJ/kg]	DCN	T_{10} [K]	$T_{90} - T_{10}$ [K]	μ_l(300 K) [mPa s]	ρ_l(300 K) [kg/m^3]
1.91	43.1	48.3	450.0	67.8	1.37	794

Table 1: Properties of the Jet-A POSF10325

2.2 Derivation of the detailed mechanism

2.2.1 HyChem Approach

As outlined in the Introduction, HyChem[42, 43] is an approach alternative to the classical multicomponent surrogate fuel approach, that is retained in this study. We briefly outline this approach here; the reader is referred to the afore-mentioned publications for details. The methodology relies on the assumption that any fuel, no matter its complexity, would decompose into a handful of components, and that it is the distribution of these pyrolysis products in the reaction zone that impacts the subsequent radical buildup and heat release rate. The pyrolysis intermediates are dominated by hydrogen (H_2), methane (CH_4), ethylene (C_2H_4), propene (C_3H_6), *iso*-butene (i-C_4H_8), 1-butene (1-C_4H_8), benzene (C_6H_6) and toluene (C_7H_8). In that sense, the combustion process can be decomposed into a fuel pyrolysis step and a subsequent oxidation of the pyrolysis products. Kinetic model for a particular real fuel can thus be obtained by merging a fuel-specific pyrolysis model comprised of a few lumped reactions, yielding the composition of the primary pyrolysis products, and a detailed foundational fuel chemistry model (C_1-C_4 kinetic mechanism). The "fuel", in that case, is a mono-component lumped species. Its pyrolysis model is derived from shock-tube and flow-reactor experiments.

The resulting HyChem model captures shock-tube ignition delay times and laminar flame speeds over a wide range of pressure, temperature and equivalence ratio. It also predicts the counterflow non-premixed flame extinction strain rates over a range of fuel dilution.

For the Jet-A considered here, the fuel breakdown is described by 6 lumped reactions, and ethylene constitutes the bulk of the pyrolysis products. The detailed mechanism for the pyrolysis products is the USCII mechanism,[40] comprised of 111 species and 784 reactions. The resulting HyChem model has already been employed in LES of spray combustion,[9] though a tabulation method was used, thus limiting the fidelity of the spray/flame modeling.

2.2.2 NO$_x$ chemistry

NO$_x$ reaction pathways can be added as a supplemental set to existing hydrocarbon mechanisms. However, the levels of NO$_x$ can rely heavily upon the production and destruction of certain radicals, such as CH.[10] Unfortunately, the chemistry of such radicals is not well understood, nor are they the main concern when deriving practical kinetic schemes employed in combustion systems. As a result, different kinetic schemes developed for the same fuel can yield quite different levels of radicals, which translate into very different NO levels, as observed and discussed, for example, in *n*-decane oxidation.[26]

Due to both a lack of experimental data and kinetic schemes available for NO$_x$ predictions in real fuels, it was decided to employ the submechanism of the Luche scheme for kerosene oxidation.[24] A total of 17 additional species and 245 additional (irreversible) reactions are added to the Jet-A HyChem model.

2.3 Derivation of the ARC mechanism

The complete reaction model will be referred to as JetA2_NOx in what follows. It is comprised of a total of 129 species and 1572 reactions described irreversibly (forward and back reactions). An analytically reduced chemistry (ARC) is then obtained from the original kinetic mechanism following three automated steps.

First, a set of targets associated with a set of canonical zero- or one-dimensional configurations is prescribed, so that the reduction can be steered towards preserving predictive accuracy of those targets. In the present case, the reduction is based on one-dimensional laminar premixed flames (PF) and zero-dimensional auto-ignition computations (AI) under atmospheric pressure, representative of the configuration of Cai *et al.*[3] The equivalence ratio (ϕ) range extends from $\phi = 0.5$ to 1.5. Targets consist of auto-ignition time (τ_{ig}), burnt gas temperature T_b, laminar flame speed s_l, main species equilibrium values, specific intermediate species profiles and integrated heat release rate. The full set of targets are reported in Table 2. Next, based upon those results, a skeletal reduction is performed where, following

Canonical test cases	Targeted ranges	Targeted constraints
PF	1 atm / 300K / ϕ = 0.8-1.3	CO CO$_2$ C$_2$H$_4$ OH NO HR
AI	1 atm / 1300-1700 K / ϕ = 0.8-1.3	CO CO$_2$ C$_2$H$_4$ OH NO HR

Table 2: List and specifications of the reduction performed with YARC.

the formalism of Turanyi,[39] unimportant species and reactions are removed from the original mechanism. This step is performed by applying the Directed Relation Graph with Error Propagation method (DRGEP), a full description of which can be found in Pepiot *et al.*[31] A skeletal mechanism comprised of 46 species and 547 irreversible reactions is eventually derived. Finally, assumptions about species and/or reaction characteristic timescales are formulated, still based upon the results of the canonical configurations, in order to reduce the stiffness of the mechanism. The Quasi Steady State Approximation (QSSA) is used in this study, and 17 species are identified by the Level of Importance (LOI) criterion[23] as being good candidates.

The resulting ARC reaction model is labelled ARC_29_JetA2NOx hereafter, and retains 29 transported species and 17 QSS as listed in Table 3. The entire reduction was performed with the automated tool YARC developed by Pepiot.[30]

Transported species	QSS species
N$_2$ H H$_2$ HO$_2$ H$_2$O H$_2$O$_2$ O O$_2$ OH CO CO$_2$	CH HCO CH$_2$ CH$_2^*$ CH$_3$O C$_2$H$_5$
CH$_3$ CH$_4$ CH$_2$O CH$_2$CO C$_2$H$_2$ C$_2$H$_4$	C$_2$H$_3$ HCCO A-C$_3$H$_5$ CH$_2$CHO C$_6$H$_5$
C$_2$H$_6$ C$_3$H$_6$ I-C$_4$H$_8$ C$_5$H$_6$ C$_6$H$_4$O$_2$ C$_6$H$_5$O	N NCO H$_2$CN CN NH HNO
C$_6$H$_6$ C$_6$H$_5$CH$_3$ POSF10325 NO HCN NO$_2$	

Table 3: Species contained in the ARC_29_JetA2NOx scheme.

The size of this reduced mechanism allows its direct implementation in the LES solver AVBP,[15] with simplified transport data, as will be described in Section 4.1.

2.4 Validations

The performance of the ARC_29_JetA2NOx is evaluated against that of the detailed mechanism JetA2_NOx in zero- and one-dimensional canonical test cases with CANTERA[17] and FlameMaster.[34] A mixture averaged formulation is employed for the transport properties of the JetA2_NOx mechanism, while for the ARC mechanism, the same simplified transport model as the one that will be used in the LES solver is employed (see Section 4.1). The constant values of species Schmidt numbers and Prandtl number are taken in the flame zone of a PF computed with complex transport. Note that the list of comparisons is not exhaustive, as the main objective is to provide tools in order to help the following discussion on LES results. To this end, emphasis is placed on global quantities.
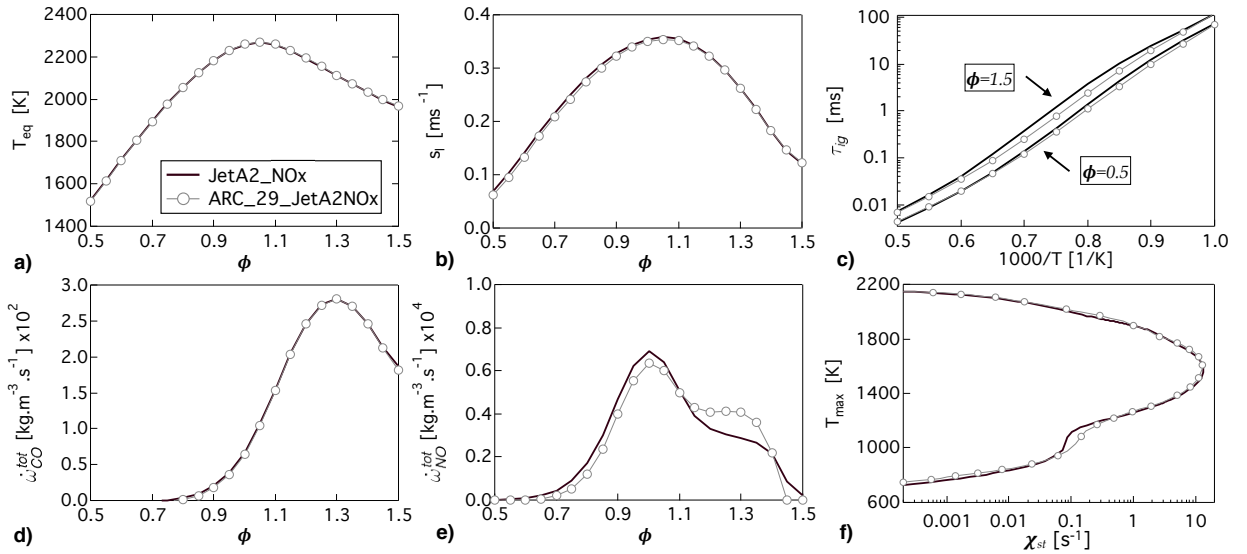

Figure 1: Global performances of the ARC_29_JetA2NOx mechanism. PF test cases: (a) T_b, (b) s_l, (d) global CO production and (e) global NO production for $T_i = 300$ K, P = 1 bar. AI test cases: (c) τ_{ig} for $\phi = 0.5$, 1.5, P = 1 bar. CF test cases: (f) S−curve for $T_i = 300$ K, P = 1 bar.

PF and AI test cases are first considered, corresponding to the canonical configurations used to derive the ARC mechanism. As expected, global quantities targeted by the reduction procedure, such as T_b, s_l and τ_{ig} are shown to be accurately recovered by the ARC_29_JetA2NOx, as seen in Fig. 1 (a)-(c). The equivalence ratio range extends beyond the targeted range, where results are still very good. In the present case, the relative error on s_l is always under 3%, except in very lean conditions where it reaches a maximum of 8%. Predicted τ_{ig} are seen to be less accurate under rich conditions, but results are still well within experimental uncertainties.

The pollutant predicting capabilities of both mechanisms are assessed by looking at the global CO/NO production through the flame front:

$$\dot{\omega}_{CO/NO}^{tot} = \int_{c<0.98} \dot{\omega}_{CO/NO} dx \tag{1}$$

Results are presented in Fig. 1 (d)-(e). We observe an excellent agreement between the original mechanism and the ARC_29_JetA2NOx results for the global production of CO, with a relative error consistently under 5% over the entire range of equivalence ratio. Global production of NO is less accurately retrieved by the ARC mechanism, with errors ranging from 10 to 40%. In light of the uncertainties discussed in Section 2.2.2, however, the results are considered satisfactory.

Finally, *a-posteriori* validations on laminar strained counterflow diffusion flames configurations (CF) are performed. Because the target application is a two-phase flow burner, the occurrence of diffusion structures is expected. S-shaped curves of maximum temperature versus scalar dissipation rate at stoichiometry, χ_{st}, are plotted in Fig. 1(f) for both detailed and ARC mechanisms. Overall, the agreement is very good. In particular, the extinction scalar dissipation rate χ_{ext} is perfectly matched by the ARC mechanism.

3. Target configuration

To the best of our knowledge, only a handful of lab-scale experimental facilities are operated with real jet fuels.[2, 3, 22] The target configuration chosen here is the lean direct injection (LDI) combustor operated at NASA Glenn.[3, 11, 20] Our choice was mainly driven by the wealth of experimental data available in terms of temperature and chemical species, allowing an accurate validation of the proposed methodology. A picture of the experimental facility is presented in Fig. 2(a) while details of the injection system are shown in Fig. 2(b). The burner consists of an axial swirler composed of six helicoidal vanes inclined at $60°$ and a PARKER pressure-swirl atomizer located in the center. The atomizer tip is located at the throat of a converging/diverging nozzle. The outer diameter of the nozzle at the combustion chamber dump plane is $D_0 = 0.025$ m. The combustion chamber has a height of 305 mm and a square section of length 50.8 mm. Quartz windows allow optical access from all sides.
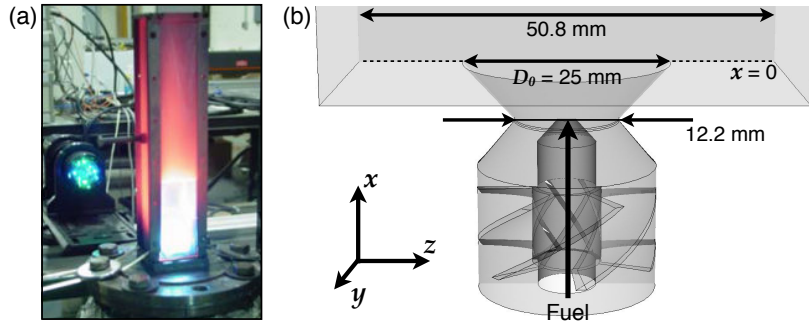

Figure 2: (a) Picture of the experimental test rig.[3] (b) Details of the injection system.

The combustor is operated at ambient conditions ($P = 1$ atm, $T = 300$ K). Air is injected with a nominal mass flow rate of 8.16 g/s through a plenum upstream of the swirler vanes while liquid Jet-A fuel is injected through the atomizer with a mass flow rate of 0.415 g/s. These conditions correspond to a lean overall equivalence ratio of 0.75. Due to the low pressure in the fuel lines, the spray is found to exhibit unstable distribution patterns.[3] Laser Doppler Velocimetry is used to measure gas velocity while Phase Doppler Particle Analyzer measurements are performed for spray velocity and droplet size distribution.[3] Gas temperature and species profiles are obtained from thermocouple and isokinetic probes, respectively.[20] This configuration has previously been studied using LES with an overall good agreement with experimental data in terms of gas velocity but discrepancies were observed in terms of spray characteristics as well as temperature and species.[8, 21, 29]

4. Numerical setup

4.1 Governing equations

4.1.1 Gas phase equations

In this study, the spatially averaged compressible Navier-Stokes equations are considered, where $\overline{\cdot}$ and $\widetilde{\cdot}$ represent Reynolds and Favre spatial filtering respectively. In the thickened flame model framework (see Section 4.1.3) and assuming dilute spray regime, the conservation equations write:

$$\frac{\partial \overline{\rho}}{\partial t} + \frac{\partial \overline{\rho \widetilde{u}_j}}{\partial x_j} = \overline{\Gamma} \tag{2}$$

$$\frac{\partial \overline{\rho \widetilde{u}_i}}{\partial t} + \frac{\partial \overline{\rho \widetilde{u}_i \widetilde{u}_j}}{\partial x_j} = -\frac{\partial}{\partial x_j}\left[\overline{p}\delta_{ij} - \overline{\tau}_{ij} - \overline{\tau}_{ij}^{sgs}\right] + \widetilde{u}_{d,i}\overline{\Gamma} + \overline{F}_{d,i} \tag{3}$$

$$\frac{\partial \overline{\rho}\widetilde{E}}{\partial t} + \frac{\partial \overline{\rho}\widetilde{E}\widetilde{u}_j}{\partial x_j} = -\frac{\partial}{\partial x_j}\left[\overline{u_i(p\delta_{ij} - \tau_{ij})} + \mathcal{E}\mathcal{F}\overline{q}_j + \overline{q}_j^{sgs}\right] + \frac{\mathcal{E}\overline{\omega}_T}{\mathcal{F}} + \overline{\Pi} + \frac{1}{2}\widetilde{u}_{d,i}^2\overline{\Gamma} - \widetilde{u}_{p,i}\overline{F}_{d,i} \tag{4}$$

$$\frac{\partial \overline{\rho}\widetilde{Y}_k}{\partial t} + \frac{\partial \overline{\rho}\widetilde{Y}_k\widetilde{u}_j}{\partial x_j} = -\frac{\partial}{\partial x_j}\left[\mathcal{E}\mathcal{F}\overline{J}_{k,j} + \overline{J}_{k,j}^{sgs}\right] + \frac{\mathcal{E}\overline{\omega}_k}{\mathcal{F}} + \overline{\Gamma}\delta_{k,F} \quad \text{for } k = 1, N_s \tag{5}$$

where ρ is the gas density, u_j is the gas j-*th* component of velocity, E is the total non-chemical energy, p is the pressure, and Y_k is the mass fraction of species k. $\mathcal{F}$ and $\mathcal{E}$ are the thickening factor and the efficiency function, respectively, introduced by the thickened flame model, and described in Section 4.1.3. τ_{ij} is the stress tensor, q_j is the heat diffusive flux and $J_{k,j}$ is the species diffusive flux evaluated with a simplified transport model. Indeed, in order to afford the direct implementation of reduced chemistries into the LES solver, transport properties are expressed in function of a constant non-dimensional Schmidt number for each species k (Sc_k) and a constant Prandtl (Pr) number. The species k diffusivities are thus given by $D_k = \mu/(\rho Sc_k)$ while the thermal conductivity is expressed as $\lambda = \mu c_p/Pr$ where μ is the dynamic viscosity and c_p is the constant pressure heat capacity. The superscript sgs indicates subgrid scale contributions arising from the LES filtering, described in Section 4.1.3. Finally, $\overline{\Gamma}$, $\overline{F}_{d,i}$ and $\overline{\Pi}$ are the liquid phase source terms detailed in Section 4.1.2.

4.1.2 Dispersed phase description

The spray is described with a Lagrangian approach where the motion of the droplets is described by the Basset-Boussinesq-Oseen equations as presented in the work of Maxey *et al.*[25] Under the assumption of small droplet diameter, small droplet Reynolds number and large density ratio between the liquid and the gas, the droplet motion equations write:

$$\frac{d\boldsymbol{x}_d}{dt} = \boldsymbol{u}_d \tag{6}$$

$$\frac{d\boldsymbol{u}_d}{dt} = \frac{1}{\tau_p}(\boldsymbol{u}_{@d} - \boldsymbol{u}_d) = \frac{\boldsymbol{F}_d}{m_d} \tag{7}$$

where $\boldsymbol{x}_d$ is the droplet position and $\boldsymbol{u}_d$ is the droplet velocity, $\boldsymbol{u}_{@d}$ is the gaseous velocity at the droplet position and m_d is the droplet mass. τ_p is the droplet relaxation time, estimated as the Stokes characteristic time:

$$\tau_p = \frac{4}{3}\frac{\rho_l}{\rho}\frac{2r_d}{C_D|\boldsymbol{u}_{@d} - \boldsymbol{u}_d|} \tag{8}$$

where ρ_l is the liquid density, r_d is the droplet diameter. C_D is the drag coefficient given in terms of the droplet Reynolds number Re_p by the Schiller and Naumann correlation[38] :

$$C_D = \frac{24}{Re_d}(1 + 0.15Re_d^{0.687}) \tag{9}$$

$$Re_d = \frac{|\boldsymbol{u}_{@d} - \boldsymbol{u}_d|2r_d}{\nu} < 800 \tag{10}$$

Droplet heating and evaporation is evaluated with an equilibrium law based on the Abramzon-Sirignano model.[1] Under the assumption of dilute spray regime, individual droplets evaporation are considered, where droplets interactions are neglected. The droplet mass and temperature are given by:

$$\dot{m}_d = \frac{dm_d}{dt} = -2\pi r_d \frac{Sh}{Sc_F}\mu_g \ln(1 + B_M)\frac{1}{\mathcal{F}} \tag{11}$$

$$\begin{aligned} \frac{dT_d}{dt} &= \frac{1}{c_L m_d}\left(-\phi_g + \dot{m}_d L_{h,F}\right) \\ &= \frac{1}{c_L m_d}\left(2\pi r_d \mu_g \overline{C}_p \frac{Nu}{Pr}(T_{g@d} - T_p)\frac{\ln(1 + B_T)}{B_T}\frac{1}{\mathcal{F}} + \dot{m}_d L_{h,F}\right) \end{aligned} \tag{12}$$

where T_d is the droplet temperature, $T_{g@d}$ is the gas temperature at the droplet position, c_L is the liquid heat capacity and $L_{h,F}$ is the latent heat of evaporation of the liquid species. Sh and Nu are the Sherwood number and Nusselt number, respectively, evaluated using the Ranz-Marshall empirical correlations.[36] Pr and Sc_F are the Prandtl number and fuel Schmidt number, respectively. μ_g and $\overline{C}_p$ are the reference condition gaseous viscosity and heat capacity estimated with the '1/3' rule between far field and droplet surface conditions. Finally, B_M and B_T are the mass and temperature Spalding number evaluated following Abramzon-Sirignano.[1] Note that, the thickening factor of the DTFLES model $\mathcal{F}$ appears on the right-hand side of Eqs. (11) and (12) in order to account for the variable change performed on the gas phase.

Finally the Lagrangian source terms appearing in the Navier-Stokes equations are computed using:

$$\overline{\Gamma} = \frac{1}{\Delta V}\sum_{d\in\Delta V}\Psi(\boldsymbol{x}_d)\dot{m}_d \tag{13}$$

$$\overline{\boldsymbol{F}_d} = \frac{1}{\Delta V} \sum_{d \in \Delta V} \Psi(\boldsymbol{x}_d) \boldsymbol{F}_d \tag{14}$$

$$\overline{\Pi} = \frac{1}{\Delta V} \sum_{d \in \Delta V} \Psi(\boldsymbol{x}_d) \left(\phi_g + \dot{m}_d h_{v,F}(T_d) \right) \tag{15}$$

where ΔV is the local control volume in which the droplet is located (usually the node cell) and $\Psi(\boldsymbol{x}_d)$ a first-order interpolation function between the particle position and the grid nodes.

4.1.3 LES subgrid scale closures

In the present study, the SIGMA eddy-dissipation model[28] is used to evaluate the subgrid Reynold stress tensor τ_{ij}^{sgs} while heat and species subgrid transports are modeled with a gradient assumption and a constant turbulent Prandtl number and turbulent Schmidt number, respectively ($Pr_t = Sc_t = 0.6$). The dynamic thickened flame model (DTFLES) is employed to model the turbulence/chemistry interaction.[5] In this approach, the flame front is thickened by a factor $\mathcal{F}$ to allow a direct resolution of the chemistry on the LES grid. Typically, about 5 grid points in the flame thickness is considered a sufficient resolution. $\mathcal{F} = 5\Delta x / \delta_{l,0}$ is thus evaluated based on a theoretical flame thickness $\delta_{l,0}$, by taking into consideration the local mesh size Δ_x. Additionally, a dynamic sensor detects regions of high heat release rate, in order to only apply the thickening factor where it is necessary. To account for the loss of flame surface induced by the flame thickening, an efficiency function $\mathcal{E}$ is introduced to provide an estimate of the subgrid flame surface wrinkling. The efficiency function formulation of Charlette *et al.*[4] is used in this work. All laminar unstrained flame characteristics appearing in this model ($\delta_{l,0}$ and $s_{l,0}$) are parameterized in function of the equivalence ratio in order to optimize the model effect to the local flow conditions.

In the present simulations, no subgrid model is employed to evaluate the gas properties at the droplet position.

4.2 Computational domain and boundary conditions

The computational domain, shown in Fig. 3, comprises the entire combustion chamber and the injection system up to the annular section upstream of the swirler. It is fully discretized using tetrahedra, with sizes varying from 0.25 mm close to the injection system to about 3 mm in the downstream part of the combustion chamber. The final computational domain contains over 4 millions nodes and 23 millions tetrahedra.
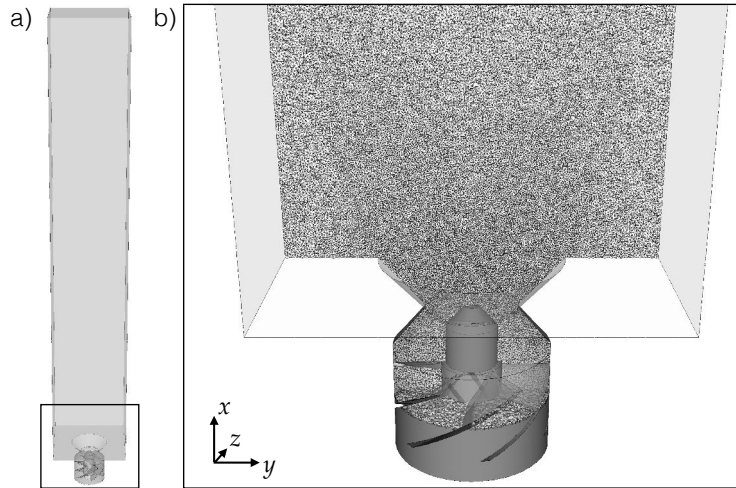

Figure 3: a) Entire computational domain and b) Mesh resolution at the vicinity of the injection system.

Simulations are performed with the compressible, massively-parallel LES solver AVBP.[15] It uses an explicit time-stepping with a third order in time and space two-step Taylor-Galerkin finite element scheme for the resolution of the convective fluxes[6] and a second order Galerkin scheme for the diffusive fluxes. Inlet and outlet boundary conditions are prescribed using the NSCBC[35] approach while walls are considered adiabatic and non-slipping.

Lagrangian particles are advanced in time with a semi-implicit Euler scheme. The interpolation of gas properties to the particle location is performed using a first order Taylor reconstruction from the closest point. A poly-disperse spray injection boundary condition is prescribed at the pressure-swirl nozzle using the FIMUR methodology.[37] Drops

are injected with a temperature of 300 K. Based on variations performed by Knudsen *et al.*,[21] a spray angle of 60° with a log-normal diameter distribution is employed in this work, with a mean of 17 μm and a standard deviation of 20 μm. An analysis of the droplet/wall interactions along the chamber walls indicates that a wide range of energy of impact C_{spl} is observed. The energy of impact is defined as C_{spl} =We.Oh$^{-2/5}$, where We is the impact Weber number We=$\rho_l d_p |u_n|/\sigma_l$ and Oh the Ohnesorge number Oh=$\mu_l/\sqrt{\rho_l \sigma_l d_p}$. Therefore, a splashing model is used, in which droplets with low energy of impact stick to the wall while droplets with large energy of impact are splashed away.[19]

5. Results

5.1 Instantaneous flame structure

The instantaneous flame structure is depicted in Fig. 4 showing contours of temperature, heat release rate, velocity and several species mass fraction in a central z-normal cut plane. The flame structure is rather complex, with a main flame zone directly fed by droplets located in front of the injector ((1) in Fig. 4(a)), and secondary reaction zones located downstream close to the combustion chamber walls ((2) in Fig. 4(a)).

Iso-contours of mixture fraction in Fig. 4 displays a rich and hot torus located in the bottom part of the IRZ. The stoichiometric iso-contours identify the main reaction zone, stabilized by the fast evaporation of the smallest droplets. This massive evaporation induces strong mixture fraction gradients, resulting in diffusion flame structures with intermittent premixed flame pockets. The top half of Fig. 4(b) shows the instantaneous field of Y_{HyChem} constructed from the sum of the Jet-A, pyrolysis products and acetylene mass fractions. Y_{HyChem} is high in the rich torus, where a large amount of CO is also observed. This testifies of the variety of diffusion flame structures that can be seen in this region.
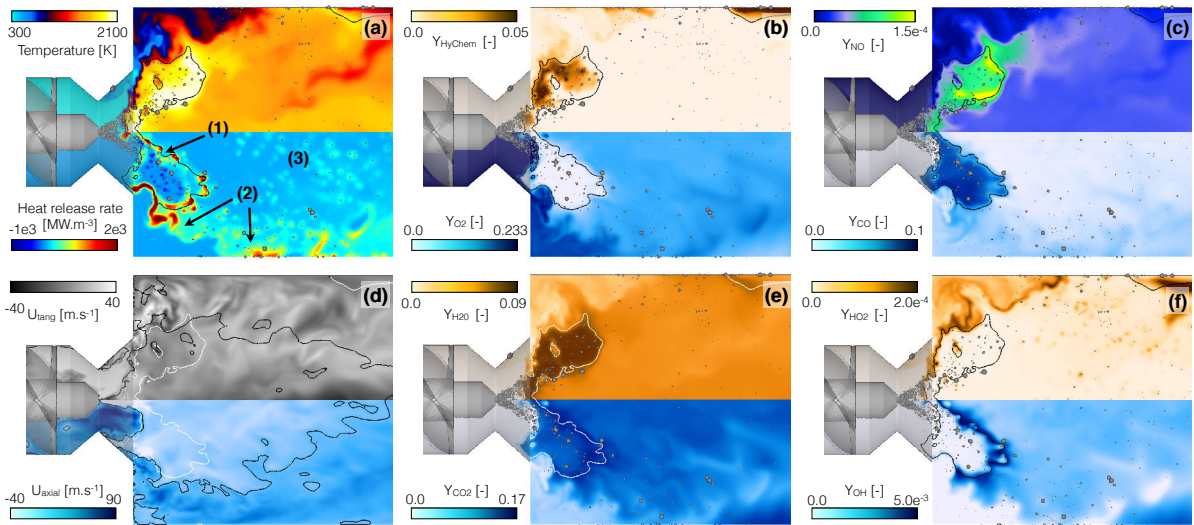

Figure 4: Instantaneous fields in a central z-normal cut plane. (a) Temperature (top) and heat release rate (bottom), (b) summed mass fractions of fuel and pyrolysis products (top) and O_2 mass fraction (bottom), (c) NO (top) and CO (bottom) mass fractions, (e) H_2O (top) and CO_2 (bottom) mass fractions and (f) HO_2 (top) and OH (bottom) mass fractions. The black iso-line indicates stoichiometry. (d) Tangential (top) and axial (bottom) components of velocity, black iso-contours delimit the IRZ while white iso-contours indicates stoichiometry.

The non-null mass fraction of H_2O, CO_2 and HO_2 upstream of the secondary reaction zones (Fig. 4(e)-(f)), in the corner of the combustor, indicates that local extinction allows dilution of the incoming air with burnt gases and pyrolysis products. As this mixture is convected along the combustion chamber walls, the increasing temperature enables the formation of a lean premixed flame front.

Finally, larger droplets are found to cross both flame fronts and to burn in an isolated droplet regime throughout the combustion chamber ((3) in Fig. 4(a)). However, the present modeling approach is not able to accurately predict the combustion regime around the droplets as it essentially occurs on a subgrid scale. Further developments are required to better capture the isolated combustion regime and its effect on pollutant formation.
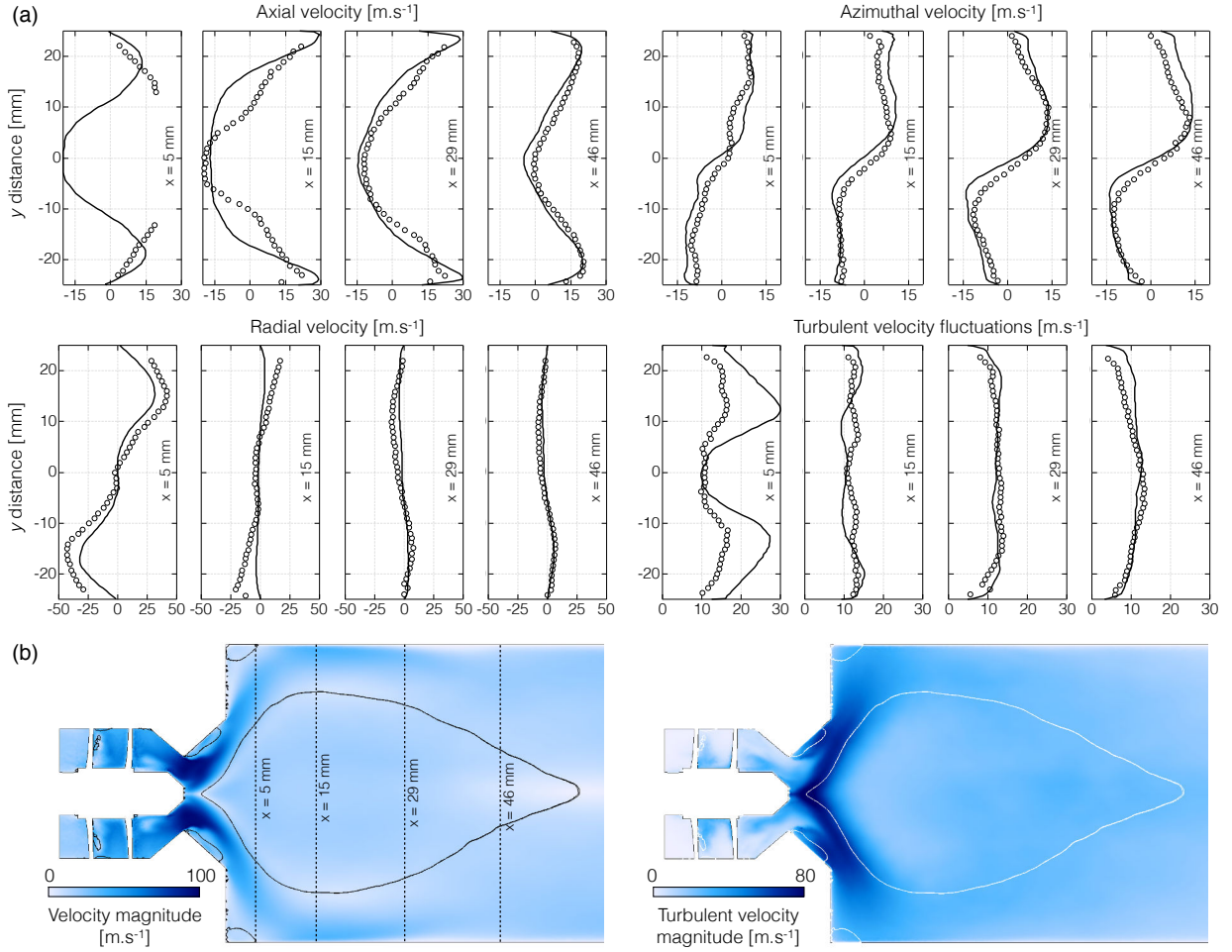
5.2 Gaseous velocity statistics

Figure 5: (a) Profiles of time-averaged mean velocity components and magnitude of the turbulent velocity fluctuations at x = 5 mm, 15 mm, 29 mm and 46 mm in reacting conditions. Symbols: experiments, black line: LES. (b) Time-averaged fields of velocity magnitude and turbulent velocity magnitude in a z-normal central cut plane. The iso-contour indicates the position of the zero axial velocity

LES statistics presented in this Section are collected during 100 ms, corresponding to about 13 flow through time of the combustor. The main flow structures are characteristic of high swirl number flows with a large opening angle of the swirled jet inducing an inner recirculation zone (IRZ). A comparison between LES and experiments is provided in Fig. 5(a). Figure 5(b) shows time-averaged velocity magnitude and turbulent velocity magnitude contours in a z-normal central plane along with the zero axial velocity iso-contour. LES predictions are found to match relatively well the experimental data, except at the vicinity of the injector where the width of the IRZ and the amplitude of the turbulent velocity fluctuations are overestimated. Experimental results suggest that the combustion process induces a strong reduction of the turbulent velocity fluctuations and a strong increase of the radial velocity component close to the injector. The IRZ is found to extend from just downstream of the pressure-swirl nozzle to about $x = 2\, D_0$. The magnitude of the negative axial velocity near the injection is also found to be large, indicating that the recirculation plays an important role in the flame stabilization mechanism. The iso-contour of zero axial velocity also highlights small outer recirculation zones in the corners of the combustion chamber as well as a small recirculation in the divergent section of the injection system.

5.3 Spray statistics

Figure 6(a) shows a comparison of LES spray statistics against experimental data and Fig. 6(b) shows the liquid volume fraction field in the central z-normal plane, constructed by projection of Lagrangian datasets. LES data are collected

from 130 instantaneous Lagrangian solutions spanning more than 50 ms. Note that to ensure a statistical convergence of the LES profiles, the data presented in Fig. 6(a) are azimuthally averaged. Radial profiles of sauter mean diameter (SMD) and mean diameter (D10) are presented first. The agreement between LES and experiments is very good at all the measured positions, with only a noticeable under-prediction of the SMD along the injector axis and of the D10 at 20 mm. The good agreement on the first profile validates the selected spray boundary conditions.[21] Large differences between the SMD and the D10 can be observed close to injector, suggesting a wide dispersion of the droplet size distribution. This is especially true close to the injector axis, where large droplets are able to penetrate the IRZ while small droplets are deflected. At increasing distance from the injector, both the SMD and the D10 increase while the two quantities are getting closer, indicating that small droplets are progressively vaporized and that the local droplet size distribution gets narrower. This effect is well predicted in the LES, showing that the present modeling approach is able to predict the droplet dispersion and evaporation.
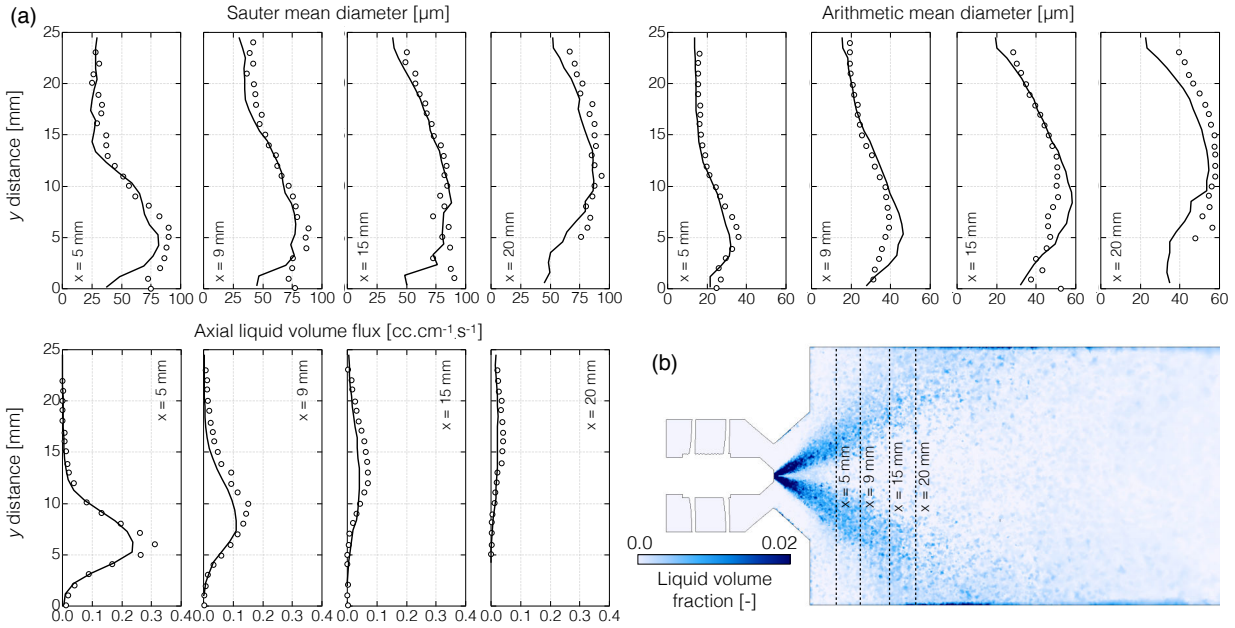

Figure 6: (a) Profiles of spray characteristics at x = 5 mm, 9 mm, 15 mm and 20 mm in reacting conditions. Symbols: experiments, black line: LES. (b) Time-averaged field of liquid volume fraction in a z-normal central cut plane.

Finally, the axial liquid volume flux is computed and compared to experiments, demonstrating that the spray angle and velocity also are well reproduced. Note that the flux is under-estimated, which is found to be due to a faster evaporation resulting of an upstream shift of the flame position compared to experiments. Figure 6(b) indicates that the spray density is rather high at the vicinity of the injector nozzle, but rapidly decreases downstream of the dump plane, validating the hypothesis of dilute spray. Finally, past 20 mm from the dump plane, high liquid volume fraction is found along the combustor walls as a result of the spray/wall interaction and it will be shown that it affects the species distribution.

5.4 Temperature and species statistics

Figure 7(a) compares experimental and LES radial profiles of temperature and major species, at several axial locations identified by vertical solid lines on Fig. 7(b), spanning the vicinity of the dump plane. H_2O and CO_2 evolutions are very well captured by the LES, even though the model predictions exhibit less asymmetry than in the experiments. Note that if some asymmetry is to be expected from the 6-vanes swirler, the LES results also suggest non-negligeable experimental uncertainties. A less well agreement is obtained on the temperature profiles, especially at the first locations, x < 20 mm. The experimental profile displays a bimodal shape at x = 20 mm, revealing the frequent presence of a flame, where a maximum temperature underprediction of about 200 K is seen in the LES. The same bimodal shape is seen on the LES profiles at x = 10 mm, suggesting that the main flame front is in fact shifted further upstream than in the experiments, as previously mentioned. An inspection of the mean stoichiometric iso-contours, superimposed with the mean fields of temperature and major species mass fractions in Fig. 7(b), confirms that the region of highest reactivity is preferably located upstream from the first profile location. Despite this apparent shift, however, the two peaks on
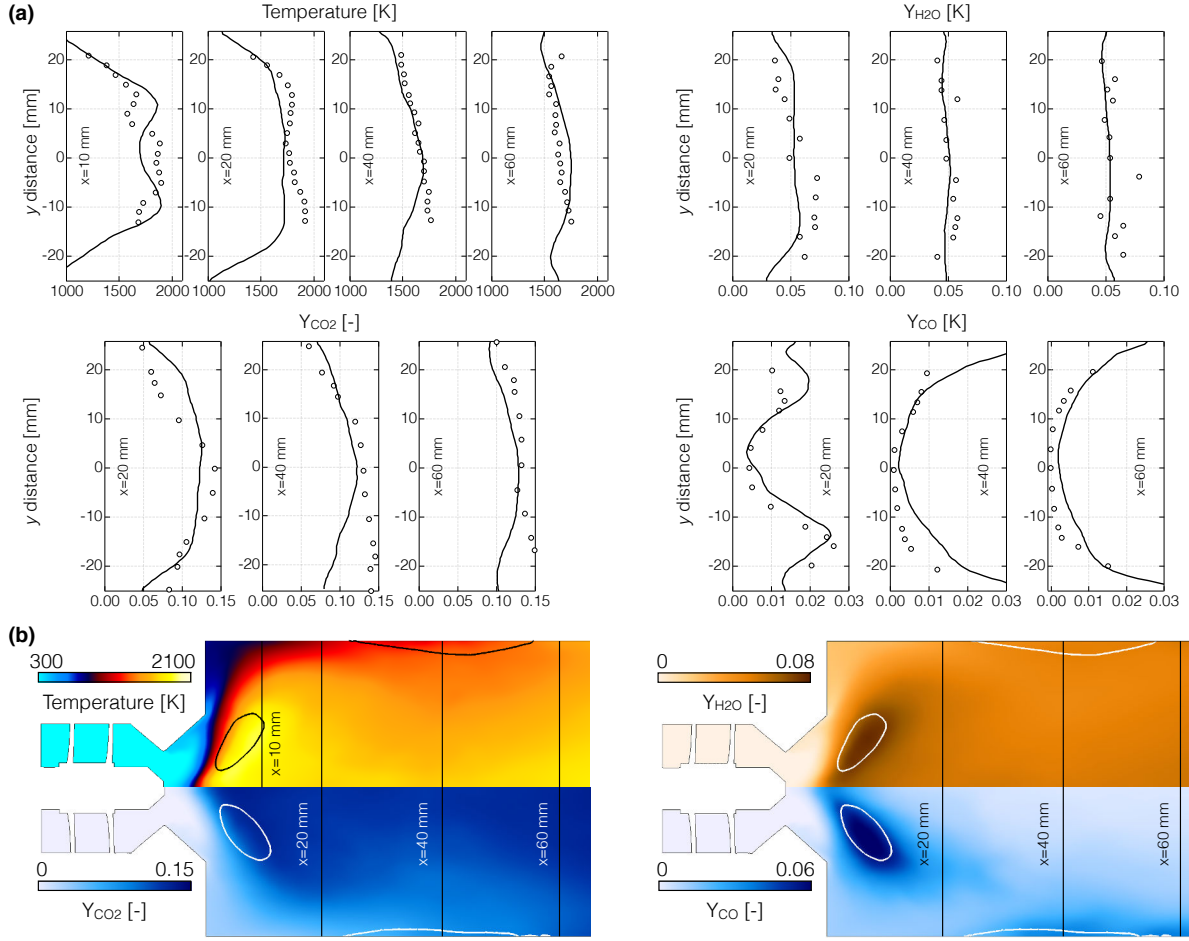
Figure 7: (a) Profiles of time-averaged temperature and selected species (CO_2, H_2O and CO) at x = 20 mm, 40 mm and 60 mm in reacting conditions. Symbols: experiments, black line: LES. (b) Time-averaged fields of temperature and selected species (CO_2, H_2O and CO) in a z-normal central cut plane. The iso-contour indicates the position of the stoichiometry

the CO profile at 20 mm, representative of the early post-flame region, are very accurately predicted by the LES. It is noted that the main flame appears lifted in both LES and experiments, which could be due to the high turbulent velocity magnitude observed close to the injector, see Fig. 5(b).

Further upstream, there seems to be an accumulation of CO species along the walls, accompanied by a decrease of temperature, in both LES and experiments. It is reminded that no heat losses are included in the simulation. These phenomena are therefore attributed to the accumulation of droplets following the jet impact, as seen on Fig. 6, leading to the formation of regions of very rich mixture fraction. Stoichiometric iso-contours along the walls, centered at x = 40 mm as seen on Fig. 7(b), confirm this analysis. For x > 60 mm, the temperature is seen to be overpredicted near the centerline. A closer examination of the experimental data indicates that the temperature at the outlet of the combustor rig is under the theoretical adiabatic value at the overall ϕ (approximately 300 K below). This difference suggests the presence of heat losses (radiation, walls, etc.) and/or incomplete combustion.

NO data are presented on Figs. 8(a) and (b). LES results are compared to experiments at several axial positions, with the last one (x = 150 mm) marking the half of the combustion chamber length. NO levels are found to be higher in the core of the IRZ, in the vicinity of the first stoichiometric iso-contours where the main flame sits, and to be significantly smaller along the walls for x < 60 mm, coinciding with low temperature regions where the jet impacts. NO levels along the centerline are seen to slightly increase with increasing distance from the injector. Overall, the main trends and levels are found to be very well captured by the LES, validating *a-posteriori* the choice of NO_x submechanism. The shape of the first profile, at x= 20 mm, is less well retrieved by the LES, with levels that are too high in the shear layer, consistent with levels found in the post-flame region and a flame front shifted towards smaller axial positions. Consistently with increasing temperature levels observed near the chamber's walls, Fig. 7(a),
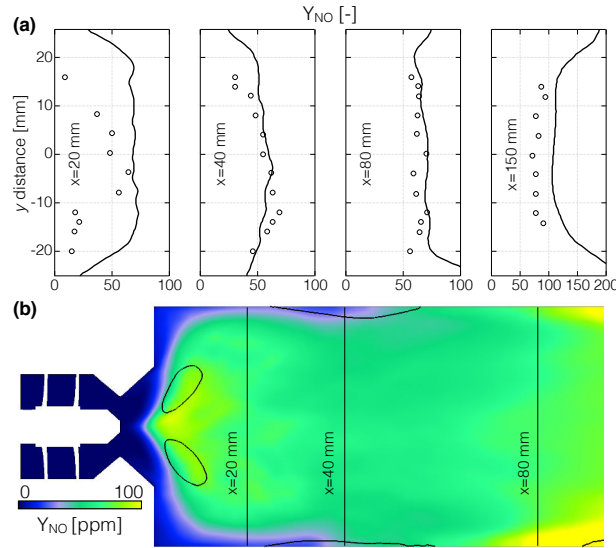
Figure 8: (a) Profiles of time-averaged NO species at $x = 20$ mm, 40 mm, 80 mm and 150 mm in reacting conditions. Symbols: experiments, black line: LES. (b) Time-averaged fields of NO species in a z-normal central cut plane. The iso-contour indicates the position of the stoichiometry

NO levels are found to increase past x > 60 mm. Since no data are available for these radial positions, however, a deeper discussion is not permitted.

6. Conclusion

A new methodology combining an ARC description and a thickened flame model with a real fuel description is proposed to improve predictive capabilities of LES in terms of flame structure and pollutant predictions. The Jet-A fuel description relies on the recently HyChem approach[43] from which an ARC is derived. Validations of the ARC in canonical configurations and successful implementation in the LES solver AVBP establish the feasibility of the methodology. This methodology is then used to simulate a Jet-A fueled lab-scale burner. A very good agreement is observed between the LES results and experimental data in terms of velocity fields and spray characteristics. Comparisons with temperature and species data demonstrate the improved predictive capabilities of the present method, when compared to previous studies. Further work will focus on the analysis of the flame structure and spray/chemistry interactions.

7. Acknowledgments

References

[1] B. Abramzon and W. Sirignano. Droplet vaporization model for spray combustion calculations. *International journal of heat and mass transfer*, 32(9):1605–1618, 1989.

[2] J. Apeloig, F.-X. d'Herbigny, F. Simon, P. Gajan, M. Orain, and S. Roux. Liquid-fuel behavior in an aeronautical injector submitted to thermoacoustic instabilities. *Journal of Propulsion and Power*, 31(1):309–319, 2014.

[3] J. Cai, S.-M. Jeng, and R. Tacina. The structure of a swirl-stabilized reacting spray issued from an axial swirler. In *43 rd AIAA Aerospace Sciences Meeting and Exhibit*, 2005.

[4] F. Charlette, D. Veynante, and C. Meneveau. A power-law wrinkling model for LES of premixed turbulent combustion: Part I - non-dynamic formulation and initial tests. *Combustion and Flame*, 131:159–180, 2002.

[5] O. Colin, F. Ducros, D. Veynante, and T. Poinsot. A thickened flame model for large eddy simulations of turbulent premixed combustion. *Physics of Fluids*, 12(7):1843–1863, 2000.

[6] O. Colin and M. Rudgyard. Development of high-order taylor-galerkin schemes for les. *Journal of Computational Physics*, 162:338–371, 2000.

[7] J. T. Edwards. Reference jet fuels for combustion testing. In *55th AIAA Aerospace Sciences Meeting*, page 0146, 2017.

[8] H. El-Asrag, A. Iannetti, and S. Apte. Large eddy simulations for radiation-spray coupling for a lean direct injector combustor. *Combustion and Flame*, 161(2):510–524, 2014.

[9] L. Esclapez, P. C. Ma, E. Mayhew, R. Xui, S. Stouffer, T. Lee, H. Wang, and M. Ihme. Fuel effects on lean blow-out in a realistic gas turbine combustor. *Combustion and Flame*, 181:82–99, 2017.

[10] C. P. Fenimore. Formation of nitric oxide in premixed hydrocarbon flames. *Symposium (International) on Combustion*, 13(1):373–380, 1971.

[11] Y. Fu, S.-M. Jeng, and R. Tacina. Characteristics of the swirling flow generated by an axial swirler. In *ASME Turbo Expo 2005: Power for Land, Sea, and Air*, pages 517–526. American Society of Mechanical Engineers, 2005.

[12] S Gallot-Lavallee and WP Jones. Large eddy simulation of spray auto-ignition under egr conditions. *Flow Turbulence and Combustion*, 96:513–534, 2016.

[13] Y. Gao, T. Lu, R. Xu, H. Wang, D. F. Davidson, C. T. Bowman, and R. K. Hanson. A reduced chemistry model for jet fuel combustion, 2015. *Personal communication*.

[14] A. Garmory and E. Mastorakos. Capturing localised extinction in sandia flame f with les–cmc. *Proceedings of the Combustion Institute*, 33(1):1673–1680, 2011.

[15] L. Y. M. Gicquel, G. Staffelbach, and T. J. Poinsot. Large Eddy Simulations of gaseous flames in gas turbine combustion chambers. *Progress in energy and combustion science*, 38:782–817, 2012.

[16] O. Gicquel, N. Darabiha, and D. Thévenin. Laminar premixed hydrogen/air counterflow flame simulations using flame prolongation of ildm with differential diffusion. *Proceedings of the Combustion Institute*, 28:1901–1908, 2000.

[17] D. G. Goodwin, H. K. Moffat, and R. L. Speth. Cantera: An object-oriented software toolkit for chemical kinetics, thermodynamics, and transport processes. http://www.cantera.org, 2017. Version 2.1.1.

[18] D. A. Goussis and U. Mass. Model reduction for combustion chemistry. *In: T. Echekki, E. Mastorakos Turbulent Combustion Modeling, Fluid Mechanics and Its Applications*, 95:193–220, 2011.

[19] N. Iafrate. *Simulation aux grandes échelles diphasique dans les moteurs downsizés à allumage commandé*. Phd thesis, IFPEN, 2016.

[20] A. Iannetti, N.-S. Liu, and F. Davoudzadeh. The effect of spray initial conditions on heat release and emissions in LDI CFD calculations. *NASA Glenn Research Center, Cleveland, OH, NASA Report No. NASA/TM—2008-214522*, 2008.

[21] E. Knudsen, Shashank, and H. Pitsch. Modeling partially premixed combustion behavior in multiphase LES. *Combustion and Flame*, 162(1):159–180, 2015.

[22] R. Lecourt, G. Linassier, and G. Lavergne. Detailed characterisation of a swirled air/kerosene spray in reactive and non-reactive conditions downstream from an actual turbojet injection system. In *ASME 2011 Turbo Expo: Turbine Technical Conference and Exposition*, pages 185–194. American Society of Mechanical Engineers, 2011.

[23] T. Lovas, P. Amnéus, F. Mauss, and E. Mastorakos. Comparison of automatic reduction procedures for ignition chemistry. *Proceedings of the Combustion Institute*, 293:1387–1393, 2002.

[24] J. Luche. *Obtention de modeles cinétiques réduits de combustion. Application à un mécanisme du kérosène*. PhD Thesis, Université d'Orléans, 2003.

[25] M. Maxey and J. Riley. Equation of motion for a small rigid sphere in a nonuniform flow. *Physics of Fluids*, 26(4):883–889, 1983.

[26] K. Moesl, J. E. Schwing, and T. Sattelmayer. Modelling NOx emissions of single droplet combustion. *Combustion Theory and Modelling*, 16(1):107–141, 2012.

[27] S. Navarro-Martinez and A. Kronenburg. LES-CMC simulations of a turbulent bluff-body flame. *Proceedings of the Combustion Institute*, 31(2):1721–1728, 2007.

[28] F. Nicoud, H. Baya Toda, O. Cabrit, S. Bose, and J. Lee. Using singular values to build a subgrid-scale model for Large Eddy Simulations. *Physics of Fluids*, 23(8):085106, 2011.

[29] N. Patel and S. Menon. Simulation of spray–turbulence–flame interactions in a lean direct injection combustor. *Combustion and Flame*, 153(1):228–257, 2008.

[30] P. Pepiot. *Automatic Strategies to Model Transportation Fuel Surrogates*. PhD Thesis, Stanford University, 2008.

[31] P. Pepiot-Desjardins and H. Pitsch. An efficient error propagation based reduction method for large chemical kinetic mechanisms. *Combustion and Flame*, 154:67–81, 2008.

[32] N. Peters. Laminar diffusion flamelet models in non-premixed turbulent combustion. *Progress in Energy and Combustion Science*, 10 (3):319–339, 1984.

[33] C. D. Pierce and P. Moin. Progress-variable approach for large-eddy simulation of non-premixed turbulent combustion. *Journal of Fluid Mechanics*, 504:73–97, 2004.

[34] H. Pitsch. FlameMaster: a C++ computer program for 0D combustion and 1D laminar flame calculations. 1996.

[35] T. Poinsot and S. K. Lele. Boundary conditions for direct simulations of compressible viscous flows. *Journal of Computational Physics*, 101:104–129, 1992.

[36] W. Ranz and W. Marshall. Evaporation from drops. *Chemical Engineering Progress*, 48(3):141–146, 1952.

[37] M. Sanjosé, J. M. Senoner, F. Jaegle, B. Cuenot, S. Moreau, and T. Poinsot. Fuel injection model for Euler–Euler and Euler–Lagrange large-eddy simulations of an evaporating spray inside an aeronautical combustor. *International Journal of Multiphase Flow*, 37(5):514–529, 2011.

[38] L. Schiller and Z. Naumann. A drag coefficient correlation. *Z. Ver. Deutsch. Ing*, 77(1):318–320, 1935.

[39] T. Turányi. Reduction of large reaction mechanisms. *New Journal of Chemistry*, 14:795–803, 1990.

[40] H. Wang, X. You, A. V. Joshi, S. G. Davis, A. Laskin, F. Egolfopoulos, and C. K. Law. USC Mech Version II. High-Temperature Combustion Reaction Model of H2/CO/C1-C4 Compounds. *http://ignis.usc.edu/USC_Mech_II.htm*, 2007.

[41] C. K. Westbrook and F. L. Dryer. Simplified reaction mechanisms for the oxidation of hydrocarbon fuels in flames. *Combustion Science and Technology*, 27:31–43, 1981.

[42] R. Xu, D. Chen, K. Wang, Y. Tao, J. K. Shao, T. Parise, Y. Zhu, S. Wang, R. Zhao, D. J. Lee, F. N. Egolfopoulos, D. F. Davidson, R. K. Hanson, C. T. Bowman, and H. Wang. Hychem model: Application to petroleum-derived jet fuels. *10th US National Meeting on Combustion, College Park, MD*, April 23-26, 2017.

[43] R. Xu, H. Wang, D. F. Davidson, R. K. Hanson, C. T. Bowman, and F. N. Egolfopoulos. Evidence supporting a simplified approach to modeling high-temperature combustion chemistry. *10th US National Meeting on Combustion, College Park, MD*, April 23-26, 2017.